



## Analysis of powder rheometry of FT4: Effect of air flow

Wenguang Nan <sup>a,b</sup>, Mojtaba Ghadiri <sup>a,\*</sup>, Yueshe Wang <sup>b</sup>

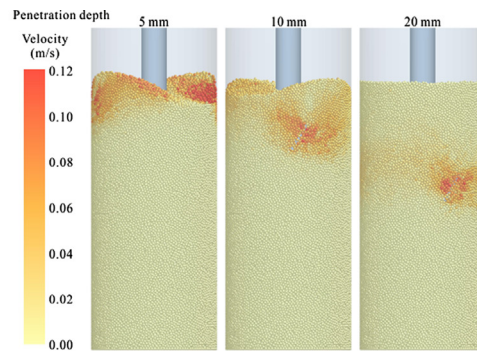
<sup>a</sup> Institute of Particle Science and Engineering, School of Chemical and Process Engineering, University of Leeds, Leeds LS2 9JT, UK

<sup>b</sup> State Key Laboratory of Multiphase Flow in Power Engineering, Xi'an Jiaotong University, Xi'an 710049, China

### HIGHLIGHTS

- Effects of gas flow and strain rate on FT4 powder rheometry are analysed.
- Bulk friction as a function of the inertial number and gas flow is quantified.
- Flow energy correlates well with the shear stresses in front of the blade.
- Flow energy and shear stresses both vary with the strain rate and gas flow.

### GRAPHICAL ABSTRACT



### ARTICLE INFO

#### Article history:

Received 29 September 2016

Received in revised form 30 November 2016

Accepted 3 January 2017

Available online 4 January 2017

#### Keywords:

DEM

Powder rheology

Powder rheometer

Flow energy

Shear stress

### ABSTRACT

Understanding of particle flow behaviour as a function of strain rate is of great interest in many items of equipment of industrial processes, such as screw conveyors, impeller mixers, and feeders. The traditional commercial instruments for bulk powder flow characterisation, such as shear cells, operate at low shear strain rates, and are not representative of unit operations under dynamic conditions. In recent years, the FT4 powder rheometer of Freeman Technology has emerged as a widely used technique for characterising particle flow under dynamic conditions of shear strain rate; yet little is known about its underlying powder mechanics. We analyse the effect of gas flow on the flow behaviour of cohesionless particles in FT4 both experimentally and by numerical simulations using the combined discrete element method (DEM) and computational fluid dynamics (CFD). The results show that the effect of gas flow on the flow energy could be described by the resultant fluid-induced drag on the particles above the blade position as the impeller penetrates the bed. The strain rate in front of the blade is mainly determined by the impeller tip speed, and is not sensitive to the gas flow and particle size. The flow energy correlates well with the shear stress in front of the blade. They both increase with the strain rate and are significantly reduced by the upward gas flow.

© 2017 Elsevier Ltd. All rights reserved.

### 1. Introduction

The study of powder flow as a function of strain rate is of great interest in fast feeding, conveying, mixing and packaging processes. At low shear strain rates powders naturally form dense structures, where the shear resistance is driven by friction and

mechanical interlocking. Techniques have long been established for characterising powder flowability for the initiation of flow under quasi-static conditions, using shear cells; based on which theories have been developed for hopper design (Carson, 2015; Jenike, 1961; Schwedes, 2003). There are extensive works reported in the literature on arching; for example cohesive arching has been analysed by Enstad (1975), and more recently mechanical arching by Tang and Behringer (2011). Nevertheless, flow inconsistency of powders is still a major challenge. Many products and processes

\* Corresponding author.

E-mail address: M.Ghadiri@leeds.ac.uk (M. Ghadiri).

require fast and reliable flow of powders at low stresses, e.g. filling dry powder inhalers, capsules, tabletting shoes, and cartons. However, neither prediction nor characterisation of their flow behaviour is achievable with quasi-static based approaches, because at high strain rates the packing density decreases and interparticle collisions and interstitial fluid drag become dominant in the shear behaviour.

Rheometry and modelling of powder behaviour under the dynamic flow conditions have received some attention in recent years (Freeman, 2007; Klein et al., 2003; Langrudi et al., 2010; Luding, 2008; Savage, 1998; Tardos, 1997; Tardos et al., 2003). Tardos et al. (2003) analysed particle flows inside a Couette device consisting of two concentric cylinders with differential rotational speeds, thus forming a shear band. Work reported in the literature so far suggests that the shear stress is constant in the slow, frictional regime, gradually increases with strain rate in the intermediate regime, and rapidly increases in the dynamic regime. In tandem to the requirement of powder flow characterisation in the dynamic range of strain rates, there is also a great need to develop techniques for measuring powder flow at low levels of consolidation stress, as relevant to feeding operations for dry powder inhalers, capsules and tabletting shoes (Pasha et al., 2013; Wang et al., 2008; Wu and Guo, 2012) and for quality by design for formulations (Leturia et al., 2014). Bulk powder flow under dynamic conditions and the associated rheology has been analysed by Campbell (2004, 2006), Delannay et al. (2007), Jop et al. (2006), Koval et al. (2009) and Pouliquen et al. (2006). The recent works of Gutam et al. (2013) and Kumar et al. (2013) show that the flow pattern even in a simple Couette geometry is more complex than previously perceived due to the secondary recirculating flow. Therefore, understanding and predicting the bulk powder flow in terms of the underlying physics, the effect of boundary conditions and material properties across the full range of shear strain rates remain a great challenge as elaborated by Mort et al. (2015).

As an alternative to the shear cell and Couette device, a rotating impeller has been used to study the powder response to shear deformation. Bruni et al. (2007) and Tomasetta et al. (2012) analysed the rheology of aerated powders in a flat-bladed paddle impeller, where the torque and shear stress were measured by a modified shear cell. They showed that the powder rheology was mainly determined by the content of fines, and proposed a rheological model using mathematical modelling based on continuum mechanics. Based on experiments and CFD simulations, Khalilitehrani et al. (2013, 2015) studied the rheology of dense granular flows in a disc impeller high shear granulator. Remy et al. (2009, 2011) carried out stress analyses of particle flow in a rotating blade mixer using DEM. They found that the normal and shear stresses were affected by the degree of polydispersity of particle size, and the shear stress was sensitive to the particle friction coefficient. Hare et al. (2011, 2013) used DEM to calculate the stress and strain rate distributions in an agitated powder bed driven by an impeller, and then characterised the particle attrition therein. They showed that for a given number of impeller rotations, the extent of breakage was independent of the impeller speed in the tested range as the bulk powder was in quasi-static regime. Hua et al. (2013, 2015) used DEM to predict the internal stress of rodlike particles in a low-speed vertical axis mixer and showed that the largest stresses within the particles occurred at their central cross-sectional plane.

These methods, however, have the rotating impeller fixed at a constant vertical position throughout the test, and hence the results obtained may not be representative of the whole particle bed as the flow properties are dependent on the bed depth. The FT4 powder rheometer of Freeman Technology (Tewksbury, UK) on the other hand has an impeller which penetrates the bed (Freeman, 2007). A twisted blade rotates at a set tip speed whilst translating in or out

of the powder bed. The input work required to drive the rotating blade into the powder bed, termed 'flow energy', is measured and advocated to represent the ease with which powder flows. This instrument has emerged as a widely used device for powder rheometry in industry and academia (Han et al., 2011; Kinnunen et al., 2014; Osorio and Muzzio, 2013; Shur et al., 2008; Vasilenko et al., 2011; Zhou et al., 2010a,b). Recently, several studies have focused on the analysis of the powder mechanics of FT4 by numerical simulations. Bharadwaj et al. (2010) used the Discrete Element Method (DEM) to simulate the effect of friction coefficient and particle shape on the resistance force and torque of the blade in FT4, and showed that the flow energy was sensitive to the particle shape and friction coefficients. However, the strain rate and the stress within the bed during the test in FT4 have not been well characterised. Therefore, the device can currently be used only for comparative testing, rather than for production process design. Hare et al. (2015) simulated the dynamics of FT4 powder rheometer for a bed of glass beads made cohesive by silanisation and plotted the flow energy with the penetration depth. They also analysed the particle stresses in front of the blade and showed the shear stress increased with the penetration depth. Regarding the constituting particles of bulk powder through which a fluid permeates, the air-particle interactions influence the powder movement. In FT4 rheometer, to evaluate the effect of aeration on the flow properties, the controlled gas flow (usually air) is optionally introduced into the particle bed through a porous stainless steel disc at the base of the testing vessel. As a result, the blade rotating and moving down into the bed will encounter less resistance and the measured flow energy will decrease. However, the fundamental effect of gas flow on the particle flow at high strain rates in FT4 rheometer has not so far been addressed.

We report on our analysis of the dynamic behaviour of the particle bed under aeration conditions using both experiments and numerical simulations with the combined discrete element method (DEM) and computational fluid dynamics (CFD). The particle bed is subjected to the standard FT4 testing procedure. By varying the permeating air velocity and tip speed, the effect of air drag on the particle flow under different strain rates is analysed. This is of particular relevance to fine and low density particles, as their motion is affected by air drag. Besides the flow energy, the strain rate and stresses within the powder bed immediately in front of the blade are also analysed. This provides a step towards understanding the dynamics of the FT4 powder rheometer in the presence of air.

## 2. Method

### 2.1. Experiments

The FT4 powder rheometer (Freeman Technology, UK) used in this work comprises a cylindrical glass vessel and a stainless steel blade which rotates and moves down and up through the powder bed at a pre-set speed (Freeman, 2007). The instrument and blade are shown in Fig. 1a and b. Polyethylene (PE) particles (density: 1000 kg/m<sup>3</sup>) supplied by Cospheric LLC, USA, are used for the experiments, with a narrow sieve cut of 500–600 µm. A photograph of the particles taken by a Scanning Electron Microscope (SEM) is shown in Fig. 2. In the experiments, the bed is initially prepared in a conditioning cycle in which the blade rotates clockwise whilst moving downward and then upward. In this way, the blade slices and lifts the particles in order to bring the particle bed to a reproducible packing state and residual stress history. After this step the downward test is carried out, in which the blade rotates anti-clockwise and moves into the powder bed while pressing down. In this way, the blade action is more compacting than slicing, resulting in shearing the bed, whilst applying normal

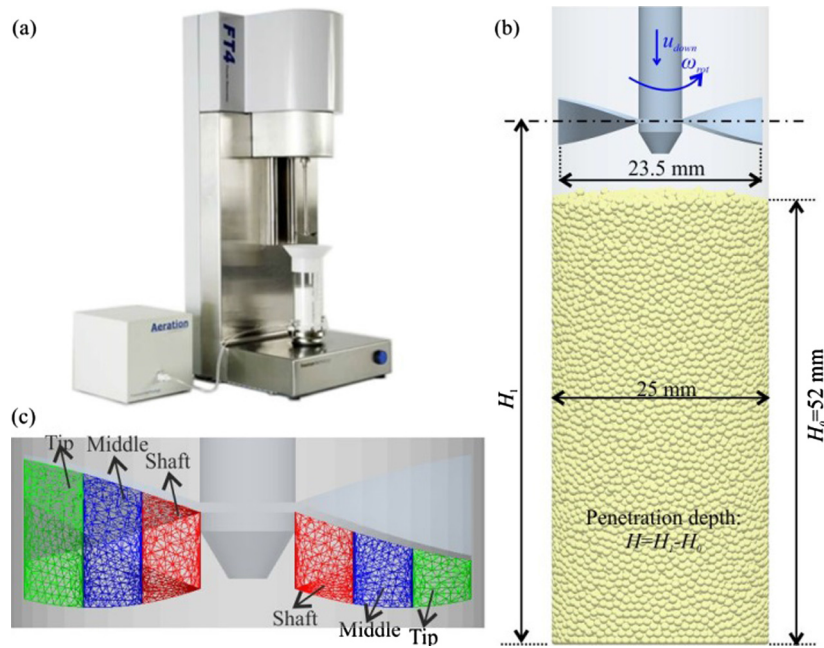


**Fig. 1.** Schematic illustration of (a) basic set up, (b) simulation system and (c) measured cells.

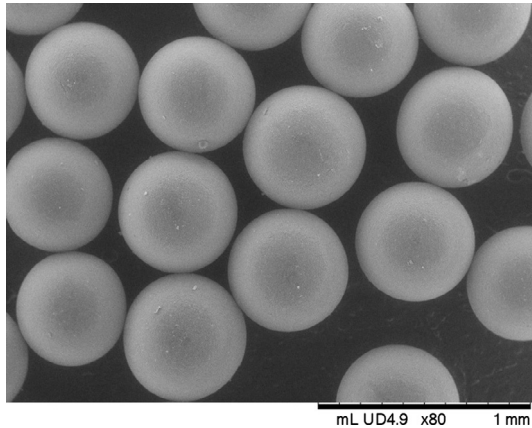


**Fig. 2.** The SEM image of polyethylene spheres (sieve cut 0.5–0.6 mm).

stresses to the particle bed by the blade. During the downward test, the torque  $T$  and axial force  $F$  required for the blade rotating and moving down are recorded. They are then used to calculate the total input work  $E$ , which is also referred to as 'Flow Energy' of the powder:

$$E = \int_0^H \left( \frac{T}{R \tan(\alpha)} + F \right) dH \quad (1)$$

where  $R$  is the radius of the blade;  $\alpha$  is the helix angle;  $H = H_1 - H_0$  is the penetration depth as shown in Fig. 1b, where  $H_1$  is the average vertical position of the blade and  $H_0$  is the initial bed height. The vertical translational velocity  $u$  and rotational velocity  $w$  of the blade are given as:

$$u = u_{tip} \sin(\alpha) \quad (2)$$

$$w = u_{tip} \cos(\alpha)/R \quad (3)$$

where  $u_{tip}$  is the tip speed, with the maximum value of 0.1 m/s. The helix angle  $\alpha$  is set by controlling the ratio of axial and angular velocities, by which the magnitude of the tip speed is defined.

In this work, the smaller glass vessel with 25 mm diameter and the corresponding 23.5 mm diameter blade are used, as shown in Fig. 1b, to enable us to also carry out numerical simulations on the exact number of particles in reasonable time. In the standard downward test, the blade moves with a constant downward speed, typically set around 0.1 m/s giving a dynamic helix angle of  $-5^\circ$ . An upward gas flow with the maximum velocity of 0.16 m/s could be optionally introduced into the powder bed through a porous stainless steel disc at the base of the testing vessel. The total flow energy corresponds to a penetration depth of 40 mm. Besides the standard downward test, a permeability test is also carried out, where the blade is only used during the conditioning cycle and kept away from the bed during the test. In the permeability test, the superficial gas velocity is increased in small steps and maintained for enough long time to eliminate the disturbance caused by the sudden increase of gas velocity. This method could also be used to measure the minimum fluidisation velocity of the particle bed. It should be noted that the permeability test in this work differs from the standard permeability test in FT4, where in the latter the particle bed is confined by a piston during the measurement. Before conducting any standard tests and permeability tests, a uniform particle bed with a height of  $H_0 = 52$  mm is generated through the conditioning cycle.

## 2.2. Simulations

The FT4 measurement process described above is also simulated by the combined approach of DEM and CFD. In this method, particles are modelled as discrete phases and their motions are tracked individually by solving Newton's laws of motion, whilst the fluid phase is still considered as a continuum (Xiong et al., 2014, 2015). The DEM-CFD numerical simulation platform is developed based on EDEM™ software provided by EDEM, Edinburgh, UK and Fluent software provided by ANSYS. For the case where the gas flow is not introduced into the system, only DEM simulation is utilised. For completeness, we only describe the key features of the simulation method as follows and further information could be found in Nan et al. (2016).

### 2.2.1. DEM for spherical particles

According to the DEM originally proposed by Cundall and Strack (1979), the movement of an individual particle for the case under consideration could be described by the translational and rotational motion:

$$m_i \frac{d\mathbf{v}_i}{dt} = \sum \mathbf{F}_{c,i} + m_i \mathbf{g} + \mathbf{f}_{pf,i} \quad (4)$$

$$\frac{d(\mathbf{I}_i \cdot \boldsymbol{\omega}_i)}{dt} = \mathbf{R}_i \cdot \left( \sum \mathbf{M}_{c,i} + \mathbf{M}_{pf,i} \right) \quad (5)$$

where  $m_i$ ,  $\mathbf{I}_i$ ,  $\mathbf{v}_i$  and  $\boldsymbol{\omega}_i$  are the mass, moment of inertia, translational velocity and angular velocity, respectively.  $\mathbf{F}_{c,i}$  is the contact force described by the Hertz-Mindlin contact model, originating from interactions with neighbouring particles or wall.  $\mathbf{f}_{pf,i}$  is the fluid-particle interaction force on the particle.  $\mathbf{M}_{c,i}$  is the contact torque, arising from the contact force and rolling friction torque.  $\mathbf{M}_{pf,i}$  is the torque due to fluid flow, but is not taken into account in this work.  $\mathbf{R}_i$  is the rotation matrix from the global to the local coordinate system in which the calculation of the rotation expressed by Eq. (5) is accomplished, and is specified as unit matrix for spherical particles.

### 2.2.2. Continuum model of fluid phase

The motion of the gas phase is described by the fluid continuity and Navier-Stokes equations based on the local mean variables over a computational cell. According to the coupling scheme Set II or Model A as reviewed by Zhou et al. (2010c), the governing equations for the incompressible fluid taking into account the effects of fluid-particle interaction can be given as:

$$\frac{\partial \varepsilon_f}{\partial t} + \nabla \cdot (\varepsilon_f \mathbf{u}) = 0 \quad (6)$$

$$\frac{\partial(\rho_f \varepsilon_f \mathbf{u})}{\partial t} + \nabla \cdot (\rho_f \varepsilon_f \mathbf{u} \mathbf{u}) = -\varepsilon_f \nabla p - \mathbf{F}_{pf} + \varepsilon_f (\mu_f + \mu_t) \nabla \cdot [(\nabla \mathbf{u}) + (\nabla \mathbf{u})^{-1}] + \rho_f \varepsilon_f \mathbf{g} \quad (7)$$

where  $\rho_f$  and  $\mu_f$  are respectively the density and viscosity of fluid.  $\mathbf{u}$  and  $p$  are respectively the velocity and pressure of fluid.  $\varepsilon_f$  is porosity in the computational cell with the volume of  $\Delta V$ .  $\mathbf{F}_{pf}$  is the volumetric fluid-particle interaction force acting on the fluid phase due to drag force  $\mathbf{f}_{d,i}$ , given as:

$$\mathbf{F}_{pf} = \frac{\sum_{i=1}^{k_c} \mathbf{f}_{d,i}}{\Delta V} \quad (8)$$

where  $k_c$  is the number of particles in the fluid cell.  $\mu_t$  is the turbulent viscosity, and set to be zero as the laminar flow is assumed here.

### 2.2.3. Particle-fluid interaction

The dominant forces acting on a particle due to the fluid flow are the pressure gradient force and drag force, given as:

$$\mathbf{f}_{pf,i} = -V_{p,i} \nabla p + \mathbf{f}_{d,i} \quad (9)$$

where  $V_{p,i}$  is the volume of an individual particle. Based on the drag on an individual particle, the scheme proposed by Di Felice (1994) is used as given by:

$$\mathbf{f}_{d,i} = 0.5 C_{d,i} \rho_f A_D |\mathbf{u}_i - \mathbf{v}_i| (\mathbf{u}_i - \mathbf{v}_i) \varepsilon_f^{2-\chi} \quad (10)$$

where  $C_{d,i}$  is the drag coefficient, and  $A_D$  is the cross-sectional area perpendicular to the fluid flow. The coefficient  $\chi$  is calculated based on the improved correlation suggested by Rong et al. (2013), which takes into account both the effects of the porosity and Reynolds number:

**Table 1**  
Material properties in simulations.

| Material property                    | Particles       | Impeller blade       | Cylindrical vessel   |
|--------------------------------------|-----------------|----------------------|----------------------|
| Density, $\rho$ (kg/m <sup>3</sup> ) | 1000            | 7800                 | 2500                 |
| Shear modulus, $G$ (Pa)              | $1 \times 10^8$ | $7.3 \times 10^{10}$ | $2.4 \times 10^{10}$ |
| Poisson ratio, $\nu$                 | 0.35            | 0.3                  | 0.3                  |

$$\chi = 2.65(\varepsilon_f + 1) - (5.3 - 3.5\varepsilon_f)\varepsilon_f^2 \exp \left[ -\frac{(1.5 - \log_{10} Re_{p,i})^2}{2} \right] \quad (11)$$

where  $Re_{p,i}$  is the particle Reynolds number, given by:

$$Re_{p,i} = \frac{\rho_f d_{V,i} \varepsilon_f |\mathbf{u}_i - \mathbf{v}_i|}{\mu_f} \quad (12)$$

where  $d_{V,i}$  is the diameter of the sphere which has the same volume as the considered particle. For the drag coefficient of particles, the equation proposed by DallaValle (1948) is used:

$$C_{d,i} = \left( 0.63 + \frac{4.8}{\sqrt{Re_{p,i}}} \right)^2 \quad (13)$$

### 2.2.4. Simulation conditions

The simulations use the same FT4 vessel and blade as the experiments, as shown in Fig. 1b. Using the poured packing method (Nan et al., 2014, 2015), approximately 36,000 spheres with a uniform distribution of diameters in the size range of 0.85–1.0 mm are generated to form a packed bed with height of 52 mm corresponding to experiment with PE particles. As the initial packed bed is almost uniform and has a low porosity of 0.41, the bed preparation procedure (namely the conditioning step) is omitted in the simulations to reduce the computational time. The tip speed is varied from 0.025 m/s to 1.0 m/s with a constant helix angle of -5°. The material properties are listed in Table 1. The friction coefficients for particle-particle and particle-blade/vessel are 0.5 and 0.25, respectively. The restitution coefficient for particle-particle is 0.6 and the same value is applied to particle-blade/vessel. For DEM-CFD simulations, air with density of 1.2 kg/m<sup>3</sup> and viscosity of  $1.8 \times 10^{-5}$  Pa s is used. The gas flow is introduced from the bottom of the vessel and three superficial gas velocities are simulated, 0.1, 0.2 and 0.3 m/s. The effect of blade motion on the air flow is considered by using the method of dynamic mesh. If not specified,

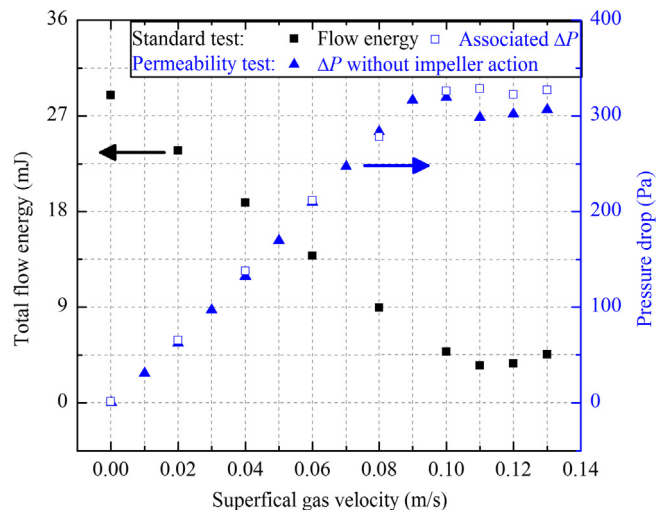


**Fig. 3.** Flow energy and associated pressure drop in the standard test (with downward impeller motion) and permeability test without impeller for PE particles ( $u_{tip} = 0.1$  m/s).

all simulation parameters discussed above are used in the following sections. The value of the restitution coefficient is based on measurement using video motion analysis. To compare the simulation results with the experimental data, 171,260 PE particles with a uniform distribution of diameter in the size range of 0.5–0.6 mm are also used in some particular cases where the extremely long computational time is required.

### 3. Experimental results

The variations of the air pressure drop,  $\Delta P$ , and total flow energy,  $E_{max}$ , with the superficial air velocity,  $u_f$ , in the standard downward test, as well as the  $\Delta P$  with the impeller out of the bed in the permeability test are shown in Fig. 3 for PE particles. Regarding the standard downward test, the pressure drop increases linearly with increasing gas velocity and then reaches a plateau. As the bed weight is partially supported by the air drag, the total flow energy decreases to the fluidised limit, following a linear trend. As for the permeability test, the pressure drop shows a similar trend as that in the standard downward test. In the packed bed state, the pressure drop has the same value in both the standard downward test and the permeability test, where in the latter case the blade is out of the particle bed. This suggests that the blade motion does not change the global porosity of the particle bed. However, when the particle bed is fluidised ( $u_f > u_{mf}$ ),

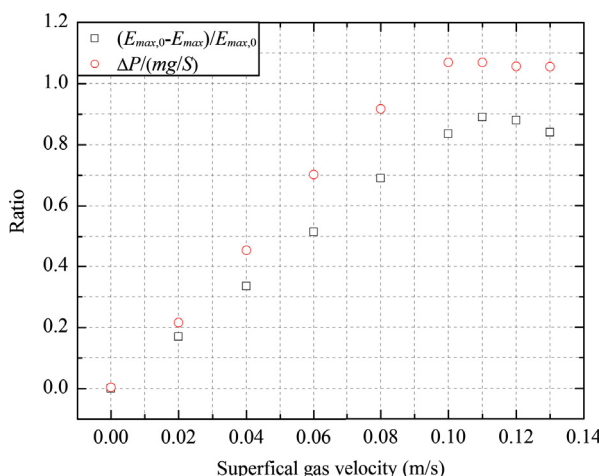


Fig. 4. Variations of  $x_E$  and  $x_P$  with the superficial gas velocity in the downward test for PE particles ( $u_{tip} = 0.1 \text{ m/s}$ ).

where  $u_{mf}$  is around 0.1 m/s, the pressure drop in the standard downward test is slightly larger than that in the permeability test. A number of factors may be responsible for the additional pressure drop, e.g. the constriction brought about by the mere presence of the impeller and the action of blade motion.

To depict the effect of gas flow on the flow energy, two ratios  $x_E$  and  $x_P$  are introduced:

$$x_E = (E_{max,0} - E_{max})/E_{max,0} \quad (14)$$

$$x_P = \Delta P/(mg/S) \quad (15)$$

where  $E_{max,0}$  is the total flow energy without air flow and  $E_{max}$  is its value where there is an upward air flow;  $x_E$  represents the relative reduction of flow energy due to the gas flow, compared to the case without air flow;  $x_P$  represents the normalised pressure drop of air flow through the bed, compared to the bed weight;  $m$  is the total mass of the particle bed;  $S$  is the cross area of the vessel. The variations of  $x_E$  and  $x_P$  with the superficial gas velocity are shown in Fig. 4.  $x_E$  and  $x_P$  show the same trend and increase with the gas velocity before reaching a plateau. The underlying cause is the interparticle contact force reduction as the air flow is increased, thus reducing the frictional work. However,  $x_P$  is larger than  $x_E$  and their difference increases with the superficial gas velocity. As  $x_E$  represents the reduced work done on shearing the bed in the presence of an upward air flow and  $x_P$  is the associated pressure drop, it is intuitively expected that they are correlated as the interparticle shear force is reduced with the bed weight partially supported by the air  $\Delta P$ .

### 4. Simulation results

Snapshots of the simulated flow pattern for spheres with the same size and properties as of PE particles and tip speed as the experiment ( $d_p = 0.5\text{--}0.6 \text{ mm}$ ,  $u_{tip} = 0.1 \text{ m/s}$ ,  $u_f = 0.0 \text{ m/s}$ ) are shown in Fig. 5. For penetration depths of 0, 1, 5 and 10 mm, where the impeller is penetrating the bed surface, the simulation shows a good visual agreement for the free surface profile with the experiment (not shown here for brevity). As the blade is driven down further, the free surface of the particle bed becomes flat when the penetration depth is larger than 20 mm, as shown in Fig. 5 (e). According to Fig. 5a-f, the impeller motion mainly affects the particles locally around the blade, whilst particles remote from the impeller are essentially stationary. The maximum particle velocity is a little larger than the tip speed, especially when the penetration depth is small where the particles have more freedom to move. This trend of flow pattern is also observed for other sim-

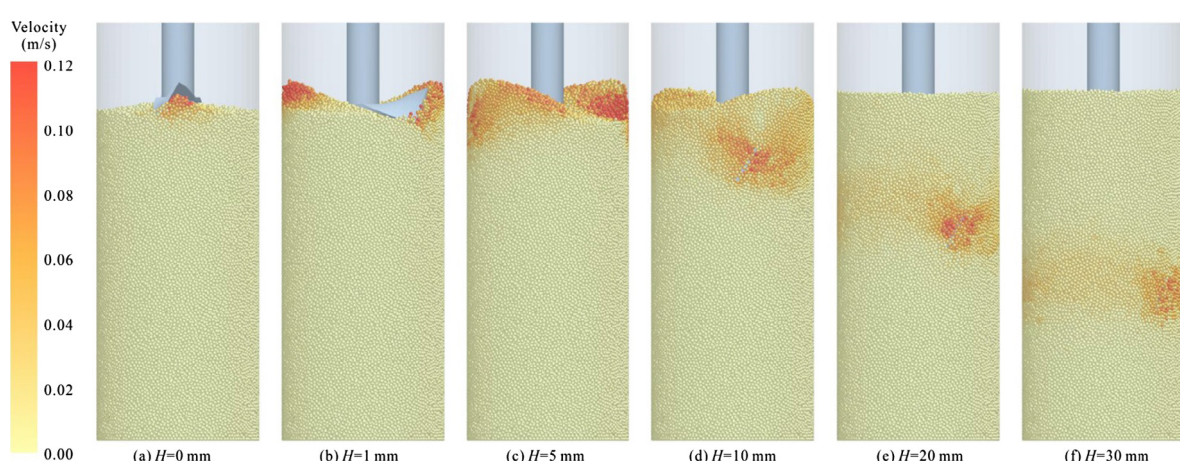
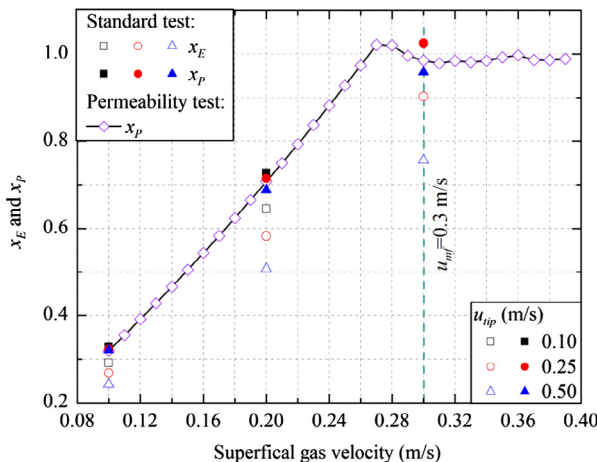


Fig. 5. The simulated flow pattern of spheres with the same properties as of PE particles for the particular case ( $d_p = 0.5\text{--}0.6 \text{ mm}$ ,  $u_{tip} = 0.1 \text{ m/s}$  and  $u_f = 0.0 \text{ m/s}$ ).



**Fig. 6.** Variations of simulated  $x_E$  and  $x_p$  with the superficial gas velocity ( $d_p = 0.85\text{--}1.0 \text{ mm}$ ).

ulation conditions. However, the total flow energy (50 mJ) in the simulation is larger than that of the experiment (29 mJ). This is attributed to the uncertainty of the value of the particle-particle friction and particle-wall friction in the simulations. Due to the extremely large computational time, the effect of friction was not investigated for the particles with diameter of 0.5–0.6 mm. In order to estimate the sensitivity of flow energy to the friction coefficients, simulations were carried out with larger particles to achieve shorter simulation times. Spheres with diameter in the size range 0.85–1.00 mm with a uniform distribution were used under tip speed of 0.25 m/s. It was observed that the flow energy could decrease to 12 mJ if the particle-particle friction coefficient was set to zero. Bharadwaj et al. (2010) and Hare et al. (2015) also showed that the flow energy was sensitive to the interparticle friction coefficient. Hence, to get a better agreement, it is possible to fine-tune the friction coefficients so that the flow energy is the same in both experimental work and numerical simulation. This approach has been adopted by Hare et al. (2015) in simulating the dynamics of cohesive particles in FT4 rheometer. However, this is not attempted here as the objective of this work is mainly to get an understanding of the effect of fluid drag on the dynamics of powder flow behaviour rather than getting a good fit with experiments. Thus, the friction coefficients discussed in Section 2.2.4 and particles size  $d_p = 0.85\text{--}1.0 \text{ mm}$  are used for all simulations in following sections, if it is not otherwise specified.

The variations of the simulated  $x_E$  and  $x_p$  for the larger particles (i.e.  $d_p = 0.85\text{--}1.0 \text{ mm}$ ) with the superficial gas velocity is illustrated in Fig. 6. In the permeability test carried out by DEM-CFD simulations, the gas velocity is increased step by step, and every increment is maintained for 0.5 s. The minimum fluidisation velocity calculated from the simulation is around 0.3 m/s, which is defined as the gas velocity where the pressure drop begins to fluctuate around the bed weight. It is close to the value of 0.27 m/s predicted by the Ergun equation. Regarding the standard test ( $u_f = 0.1, 0.2$  and  $0.3 \text{ m/s}$ ) shown in Fig. 6, the pressure drop in the packed bed state is the same as that in the permeability test. Meanwhile,  $x_p$  is clearly larger than  $x_E$  in all cases. These results are in line with the experimental results for the smaller PE particles shown in Figs. 3 and 4.

The difference between  $x_E$  and  $x_p$  also increases with the tip speed. As discussed above, the blade motion provides local agitation, compacting and slicing the bed, resulting in particle shearing in front of blade. As  $x_E$  represents the interparticle frictional work, the impeller tip speed has more effect on  $x_E$  than  $x_p$ , leading to the trend of  $x_E$  increasing faster than  $x_p$ . It also indicates that  $x_E$  is more

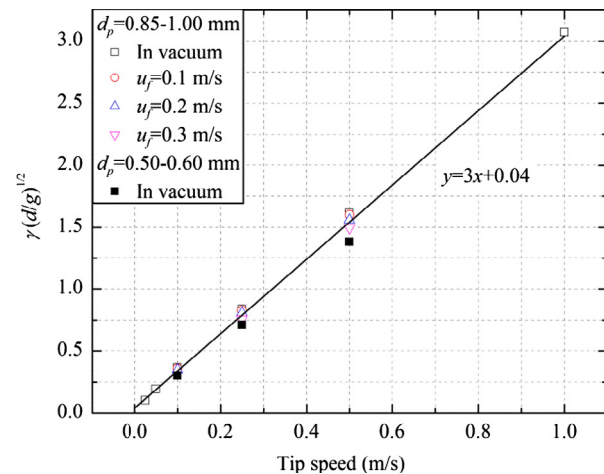


**Fig. 7.** The relationship between the simulated non-dimensional strain rate and tip speed.

sensitive to the strain rate which is representative of the impeller tip speed. We consider the strain rate immediately in front of the blade, within the measurement cells that span the width of the blade, as shown in Fig. 1c. Similar to the method suggested by Remy et al. (2009, 2011) and Hare et al. (2015) the measurement cell size is about 5–6 particle diameter. Based on the velocity gradient of particles, the strain rate in the measurement cells is given as:

$$\gamma_{ij} = \frac{1}{2} \left( \frac{\partial u_i}{\partial x_j} + \frac{\partial u_j}{\partial x_i} \right) \quad (16)$$

$$\gamma = 2 \sum \gamma_{ij} \gamma_{ij} \quad (17)$$

where  $\gamma_{ij}$  is the strain rate tensor;  $\gamma$  is the second invariant of the strain rate tensor.  $\gamma$  can be normalised according to Tardos et al. (2003), where the non-dimensional shear strain rate  $\gamma_0$  is defined as:

$$\gamma_0 = \gamma \sqrt{d_p/g} \quad (18)$$

As the strain rate changes little with the penetration depth, the time averaged value is used here. The normalised strain rate at the tip region and the shaft region is about 1.3 and 0.7 times the cell-average value, respectively. This is not shown here for brevity but as intuitively expected, the normalised strain rate is largest in the tip region and lowest in the shaft region. The variation of the sim-

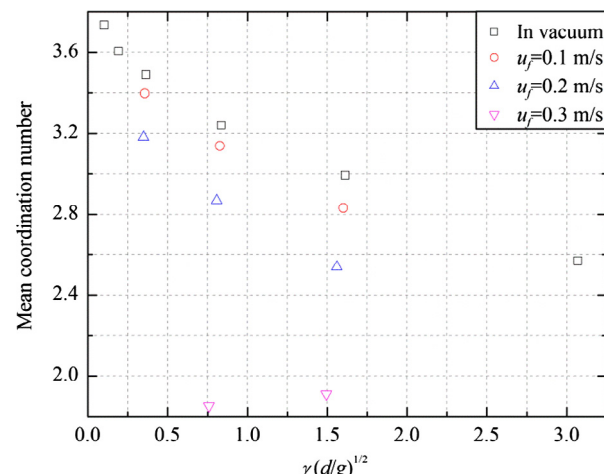


**Fig. 8.** The relationship between the simulated non-dimensional strain rate and mean coordination number.

ulated strain rate with the tip speed is shown in Fig. 7, where the results for the particles with diameter of 0.5–0.6 mm are also included. It shows that the strain rate is mainly determined by the tip speed, and is independent of the particle size and superficial gas velocity. The trend is linear with a slope of around 3.

The strain rate also has a strong influence on the microscopic structure of the particle bed in terms of the coordination number which is defined as the number of particles in contact with the considered particle. Here, the mean coordination number within the measurement cells is shown in Fig. 8. It decreases with the strain rate, as the particle bed is more agitated by the faster impeller speed. Furthermore, for a specific tip speed, the mean coordination number reduces by the introduction of gas flow. The strain rate changes only very slightly with the gas velocity, suggesting that the microstructure of the bed as described by the coordination number is affected strongly by the strain rate and the permeating gas flow.

#### 4.1. Flow energy

The evolution of the simulated flow energy with the penetration depth and impeller tip speed is given in Fig. 9, calculated from Eq. (1). In the case presented here, the term ‘vacuum’ is used to indicate that the flow energy is calculated without considering the fluid drag. The results show that it increases with depth with a

power index greater than unity, due to the increase of the rotational and translational resistances with the depth. It also increases with the tip speed. However, the increment is not significant when the tip speed is below 0.1 m/s. The effect of air flow on the evolution of flow energy for the tip speed of 0.25 m/s is shown in Fig. 10, where the case with  $u_f = 0.0 \text{ m/s}$  is also given and compared. In contrast to the case of ‘vacuum’, the fluid drag is taken into account here, but there is no fluid flow permeating through the bed. The flow energy of the system with  $u_f = 0.0 \text{ m/s}$  is the same as that in vacuum, because the particles are large and the tip speed is small, hence the air drag has little influence. To reduce the computational time, the DEM simulation for the case of vacuum is used for comparison with those for the gas flow, as the same flow energy is obtained for both systems  $u_f = 0.0 \text{ m/s}$  and ‘vacuum’. The case of vacuum does not obviously exist in reality; however the case without air flow can be represented by it, as the particles are unaffected by the fluid drag for  $u_f = 0.0 \text{ m/s}$  and there is no difference in the flow energy. In this way, the simulation time is much shorter as the coupling DEM-CFD simulation is time consuming. The flow energy is significantly reduced by the gas flow, and at gas flow rates near fluidised state it is almost negligible as expected. It should be noted that the flow energy is always larger than zero as there is always resistance for the blade to displace the bed even if it is fluidised. The contribution of the rotational resistance to the total flow energy is around 90% in all cases.

At any given height the prevailing stress state depends on the bed weight above the blade. This causes resistance to shear deformation. Here, the flow energy is normalised by the potential energy of the particle bed above the blade  $m_b g H$ , where  $m_b$  is the total mass of particles above the blade, and  $H$  is the penetration depth. The simulation results are shown in Fig. 11, where the non-dimensional flow energy is given as a function of the penetration depth. It decreases sharply first when the penetration depth is less than 10 mm, and then gradually to a plateau as shown in the zoomed part. However, for the case of  $u_f = 0.3 \text{ m/s}$ , the non-dimensional flow energy always decreases with the penetration depth, but at a very slow rate when the penetration depth is larger than 20 mm. At great depth the normalised flow energy is almost invariant with depth. Thus, the non-dimensional flow energy is averaged for the last 20 mm of the penetration depth and its dependence on the strain rate is shown in Fig. 12. For the cases of vacuum, the non-dimensional flow energy increases linearly with the strain rate. For the cases of gas flow, a similar trend is observed albeit with three data points. Furthermore, the flow

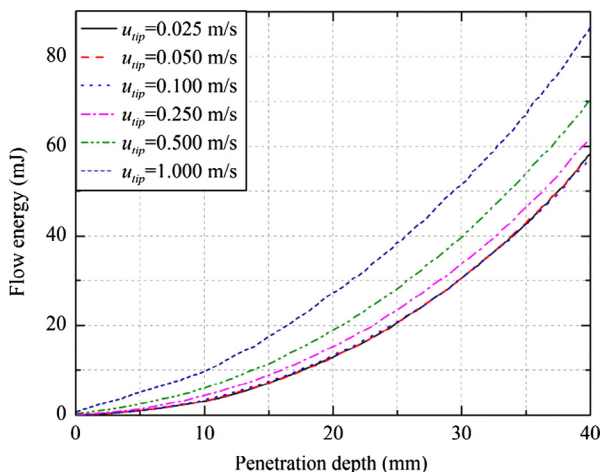


Fig. 9. Variations of the flow energy with the penetration depth in vacuum.

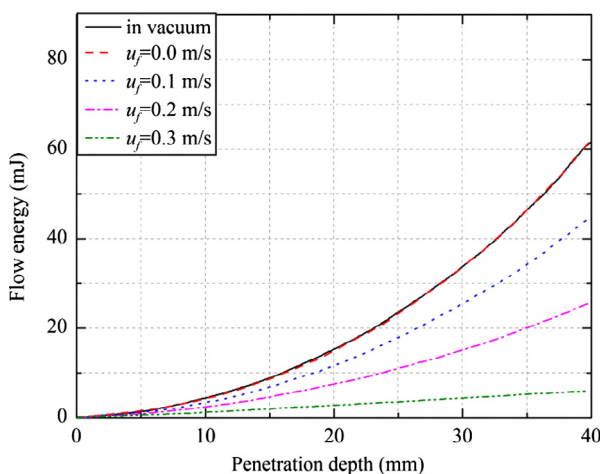


Fig. 10. Variations of the flow energy with the penetration depth in air flow with  $u_{tip} = 0.25 \text{ m/s}$ .

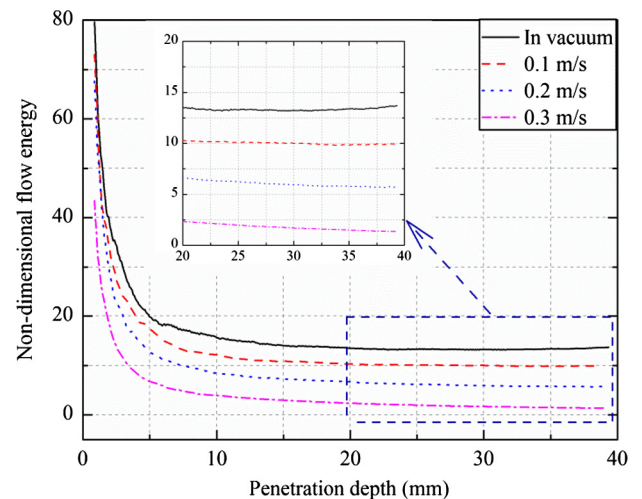


Fig. 11. Simulation result of the evolution of the non-dimensional flow energy with the penetration depth for  $u_{tip} = 0.25 \text{ m/s}$ .

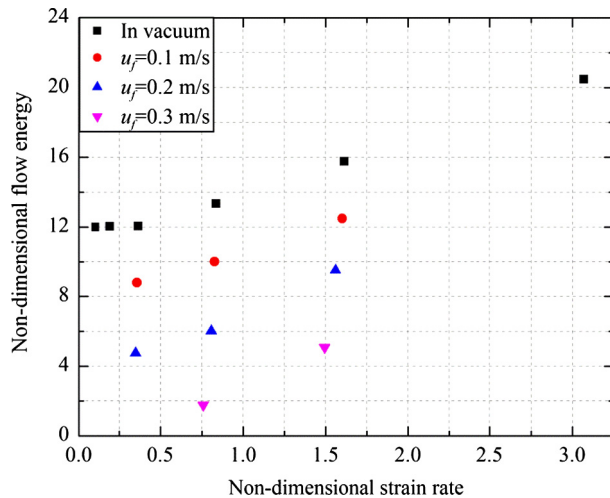


Fig. 12. Simulation results of the variation of the flow energy with strain rate for different gas flow rates.

energy decreases with the superficial gas velocity, and with a slight change in the strain rate. For a given specific superficial gas velocity, the flow energy always increases with the tip speed, even when the particle bed is near fluidised state. It is noteworthy that in the case of particles in vacuum, i.e. not affected by air drag, the flow energy is almost independent of the strain rate at very low strain rates.

As discussed above, the pressure drop contributes notably to the reduction of the flow energy. To further explore its effect on the flow energy, another parameter is introduced here:

$$x_f = \left( \int_0^H \frac{f_{pf,z}}{m_b g} dE_0 \right) / E_0 \quad (19)$$

where  $f_{pf,z}$  is the summation of fluid induced forces on all particles above the blade position resolved in the vertical direction, and this is equivalent to  $\Delta P \times S$  for the position above the blade;  $m_b$  is the bed mass above the blade;  $dE_0$  is the incremental flow energy for the impeller penetrating the incremental height  $dH$  in vacuum;  $E_0$  is the total flow energy in vacuum at penetration depth  $H$ . Considering a simple concept where the incremental flow energy  $dE_0$  is reduced by a factor  $f_{pf,z}/m_b g$  to account for the reduction of the normal interparticle contact force, which is responsible for the magnitude of the shear traction at interparticle contacts,  $x_f$  represents the

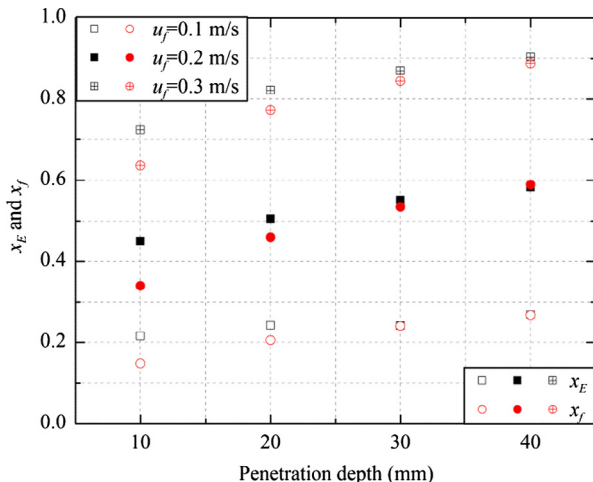


Fig. 13. Variations of simulated  $x_E$  and  $x_f$  at different penetration depths for  $u_{tip} = 0.25 \text{ m/s}$ .

reduced flow energy due to fluid induced force on particles as compared to the one in vacuum. It is plotted as a function of the penetration depth in Fig. 13 along with  $x_E$ .  $x_f$  increases with the penetration depth and then approaches a plateau.  $x_E$  shows a similar trend as that of  $x_f$  with the increase of the penetration depth, particularly at great depths. There is a notable difference between  $x_E$  and  $x_f$  for the penetration depths less than 20 mm, as the particle flow is not stable and the particle inertia may have some effect. However, with the increase of the penetration depth, the deviation is much reduced, especially at  $H = 30$  and 40 mm. This trend suggests that the effect of gas flow can be accounted for by a multiplying factor reducing the incremental flow energy in vacuum when an upward drag prevails. Another noteworthy conclusion is that the flow energy measurement is best to be made at great depths, discarding the contribution from the initial heights.

#### 4.2. Stress analysis

Similar to the strain rate analysis presented above, the stress analysis is also carried out for the region immediately in front of the blade, within three measurement cells shown in Fig. 1c. Here, the stress tensor is given by:

$$\sigma_{ij} = \frac{1}{V} \left( \sum_{p \in V} m_p \delta v_i \delta v_j + \sum_{c \in V} f_{ij} \cdot r_{ij} \right) \quad (20)$$

where  $V$  is the cell volume;  $m_p$  is the mass of particle  $p$  which is within the cell;  $\delta v_i$  and  $\delta v_j$  are the fluctuation velocities of particle  $p$  within the cell;  $f_{ij}$  is the contact force at contact  $c$  which is within the cell and  $r_{ij}$  is the corresponding branch vector. The first term is the sum of the kinetic energy fluctuations, and the second term is due to the contact forces between particles. Based on the stress tensor, the three principal stresses could be calculated: major one  $\sigma_1$ , intermediate one  $\sigma_2$  and minor one  $\sigma_3$ . The normal stress  $p$  and shear stress  $\tau$  are then given as:

$$p = \frac{\sigma_1 + \sigma_2 + \sigma_3}{3} \quad (21)$$

$$\tau = \frac{\sqrt{(\sigma_1 - \sigma_2)^2 + (\sigma_1 - \sigma_3)^2 + (\sigma_2 - \sigma_3)^2}}{\sqrt{6}} \quad (22)$$

The evolution of the normal and shear stresses for the particle flow in vacuum with  $u_{tip} = 0.25 \text{ m/s}$  is shown in Fig. 14. The normal stress increases with the penetration depth as intuitively expected. The evolution of shear stress shows the same trend as of the normal stress. With the increase of the gas velocity for the cases  $u_f < u_{mf}$ , the stresses are significantly reduced. Nevertheless, the trend of data is the same as in Fig. 14 and is not shown here for brevity. However, when the gas velocity is 0.3 m/s (i.e. around fluidisation), the evolution is much different, as shown in Fig. 15. With the increase of the penetration depth, the normal and shear stresses firstly increase, but then gradually reach a plateau when the penetration depth is greater than roughly 10 mm. Moreover, both cases of vacuum and gas flow show that the radial distribution of stresses is not uniform. The normal and shear stresses are both largest in the tip region and smallest in the shaft region. This trend is similar to the distribution of shear strain rate along the blade length.

The shear stress shows the same trend as the normal stress, suggesting that the relationship between them could be quantified by a simple bulk friction coefficient  $\mu_e = p/\tau$ . Similar to the rheological analysis of dense particle flow, the inertial number  $I$  (MiDi, 2004) is used to describe the shear stress regime:

$$I = \gamma d \sqrt{\rho_p/p} \quad (23)$$

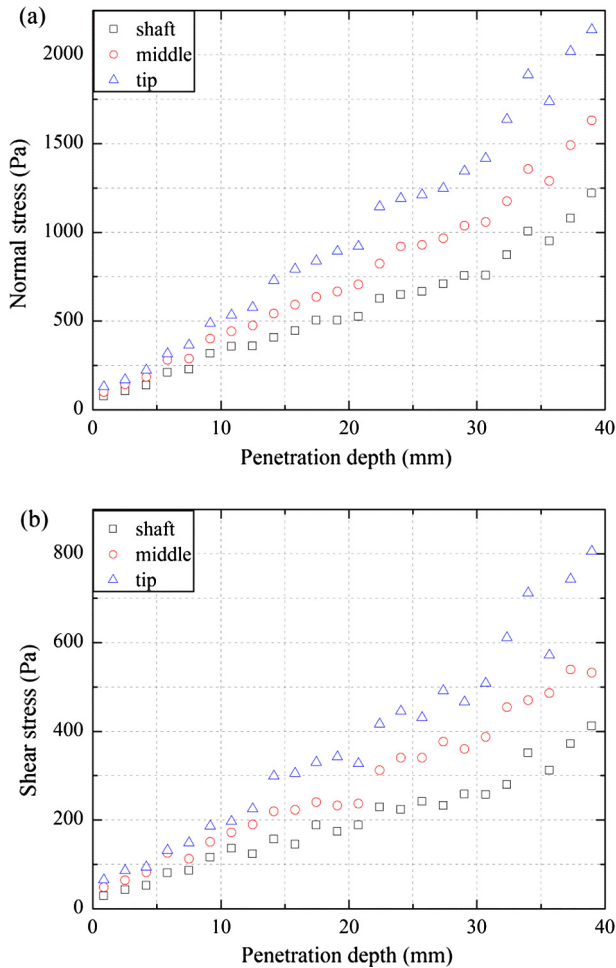


**Fig. 14.** The evolution of (a) normal stress and (b) shear stress with the penetration depth for  $u_{tip} = 0.25 \text{ m/s}$  in vacuum.

It is noteworthy that the non-dimensional strain rate shown in Eq. (18),  $\gamma(d/g)^{0.5}$ , could be considered as a simplified version of the inertial number, assuming that  $p$  equals to  $\rho_p dg$ , i.e. as relevant to the quasi-static flow regime. The inertial number is interpreted as the ratio between the macroscopic deformation timescale ( $1/\gamma$ ) and the inertial timescale  $d/(p/\rho_p)^{0.5}$ , which is the characteristic particle-level response time of a particle subjected to the normal stress  $p$  (MiDi, 2004). The flow regime could be classified into quasi-static (large  $p$  or small  $\gamma$ , where the particle inertia is negligible), intermediate dense flow, where  $\mu_e$  increases approximately linearly with  $I$ , and rapid flow (small  $p$  or large  $\gamma$ ), where the shear stress is due to particle collisional process (da Cruz et al., 2005; Jenkins, 2006; MiDi, 2004).

It is interesting to note that based on Eq. (23), the inertial number decreases with the blade penetration depth due to the increased normal stress. The variations of the bulk friction coefficient are shown in Fig. 16 as a function of the inertial number which is averaged from the depth of 20 mm downwards. For the cases without gas flow, the bulk friction coefficient (where the impeller tip speed  $u_{tip} > 0.1 \text{ m/s}$ ) increases almost linearly with the inertial number (observable on a linear abscissa), indicating that the particle flow is in the intermediate dense flow regime. However, for the tip speeds less than 0.1 m/s (i.e.  $I < 0.03$ ), the bulk friction coefficient is not sensitive to the inertial number, as shown by the first three data points for the case of in vacuum in Fig. 16, albeit with a limited number of data points due to the extremely long simulation times. This suggests that the particle flow is in

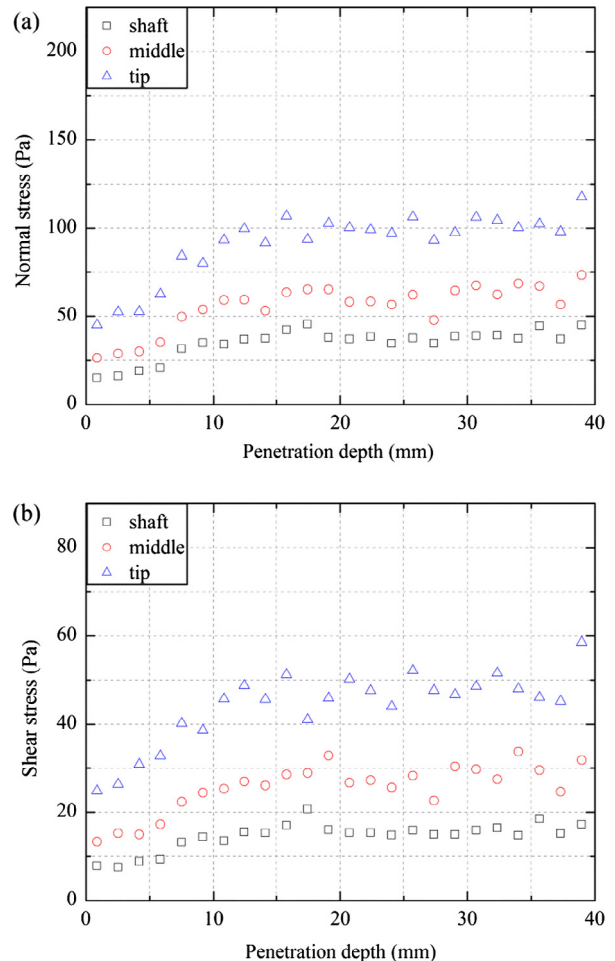


**Fig. 15.** The evolution of (a) normal stress and (b) shear stress with the penetration depth for  $u_{tip} = 0.25 \text{ m/s}$  and  $u_f = 0.3 \text{ m/s}$ .

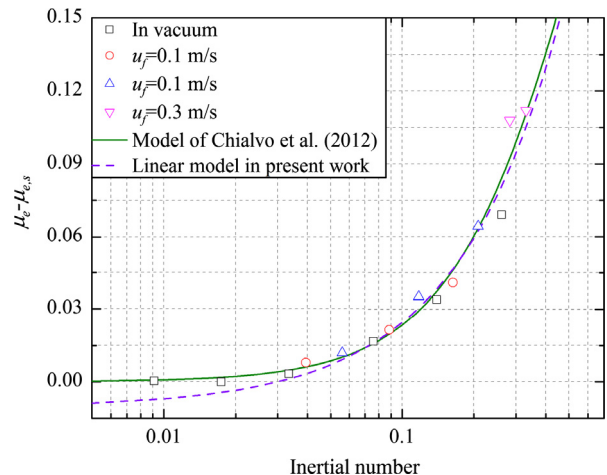


**Fig. 16.** The functional relationship of the effective bulk friction coefficient with the inertial number.

the quasi-static flow regime. As the gas flow is introduced, the inertial number increases due to the reduction of normal stress, resulting in an increase of the bulk friction coefficient. This is intuitively unexpected, but the trend arises because the normal stress is reduced much more than the shear stress when there is an upward gas flow. When the superficial gas velocity is near  $u_{mf}$ , a

much larger bulk friction coefficient is observed. Chialvo et al. (2012) proposed a model of the bulk friction coefficient, combining the asymptotic relations in the three flow regimes of quasi-static, intermediate and inertial. For the quasi-static and intermediate regimes, their model is given by Eq. (24), which is similar to that of Jop et al. (2006).

$$\mu_e = \mu_{e,s} + \frac{\alpha}{(I_0/I)^\beta + 1} \quad (24)$$

where  $\mu_{e,s}$  is the bulk friction coefficient in the limit of quasi-static regime,  $I_0$  and  $\beta$  are constant parameters for the transition from quasi-static to rapid flow.  $\mu_{e,s}$  depends on the friction coefficient between particles, whilst  $\alpha$ ,  $I_0$  and  $\beta$  are parameters independent of particle friction. In the work of Chialvo et al. (2012),  $\mu_{e,s}$  increases with the friction coefficient between particles, and the proposed friction-independent parameter values are:  $\alpha = 0.37$ ,  $I_0 = 0.32$ ,  $\beta = 1.5$ . In the present simulations, the bulk friction coefficient is described very well by the model of Chialvo et al. (2012), as shown in Fig. 16, using the following values:  $\mu_{e,s} = 0.34$ ,  $\alpha = 0.37$ ,  $I_0 = 0.6$ ,  $\beta = 1.5$ . It is noteworthy that due to limited data of the effect of particle-particle friction, the value of friction-independent parameter may be not very accurate, so we use the same values of  $\alpha$  and  $\beta$  as proposed by Chialvo et al. (2012) while changing  $I_0$ . In fact, because of the power law relation given by Eq. (24), there is not unique best fit, and  $I_0 = 0.4$  leads to  $\alpha = 0.24$ , while  $I_0 = 0.8$  leads to  $\alpha = 0.54$  for the same best correlation coefficient. Converting Fig. 16 to the linear abscissa (not shown here for brevity) reveals that the bulk friction coefficient in the intermediate regime is in fact very linear with the inertial number and can be well described by a simpler model, given as:

$$\mu_e = \mu_{e,s} + a(I - I_s) \quad (25)$$

where  $a$  is the slope of  $\mu_e - I$  curve and  $I_s$  is the value of the inertial number for transition from quasi-static to the intermediate regime. The parameters in the linear model are  $a = 0.35$  and  $I_s = 0.03$  and the quasi-static bulk friction coefficient  $\mu_{e,s} = 0.34$ .

Similar to the flow energy, the shear stress is normalised by the bed weight above the blade position, i.e.  $\tau/(m_bg/S)$ . Its average value for the penetration depths larger than 20 mm is shown in Fig. 17. For all the cases analysed here, the shear stress increases with the strain rate at large strain rates and the trend is almost linear. However, for the case of particles in vacuum, at the low strain rate, the shear stresses show a small decrease. The underlying cause is unknown, but is likely due to conjecture described below. The shear stress is significantly reduced by the gas flow with a slight change in

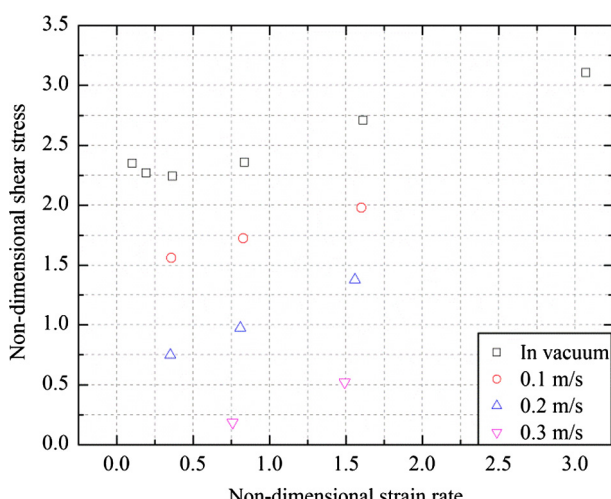


Fig. 17. The relationship between the shear stress and strain rate.

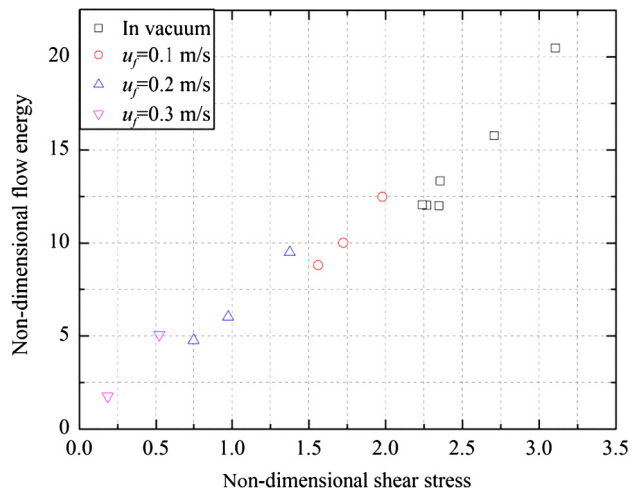


Fig. 18. The relationship between the flow energy and shear stress.

the strain rate. This trend suggests that the shear stress is the outcome of the competition between the strain rate and coordination number as shown in Fig. 8. At very low strain rates such as the first three data points, or for the cases of gas flow where the strain rate changes little with the gas velocity, the variation of the shear stress is mainly dominated by the coordination number. In this condition, the decrease in the coordination number due to the larger tip speed or gas flow could reduce the shear stress. Conversely, the shear stresses are mainly determined by the strain rate, leading to the increase of the shear stress with the strain rate.

By comparing Figs. 12 and 17, the flow energy and shear stresses show similar trends in the variations with the strain rate. They describe the powder bed rheology for cohesionless free flowing powders. Moreover, the results clearly show that there exists a direct relationship between the flow energy and shear stress, as illustrated in Fig. 18. The flow energy increases with the shear stress in a linear trend for both cases of vacuum and gas flow. In summary, the flow energy as determined by FT4 is well correlated with the shear stress. However, as the shear stress is a function of the shear rate, FT4 results represent the dynamic conditions in the intermediate flow regime, where the bulk friction coefficient is a linear function of the inertial number.

## 5. Conclusions

The rheological behaviour of polyethylene spherical particles subjected to shearing flows by an impeller in the presence of an upward gas flow has been analysed under high shear strain rates using the FT4 instrument by a combination of experimental measurements and DEM-CFD simulations. The bulk particles are subjected to the standard downward test procedure of FT4 rheometer, where a rotating blade is driven into the particle bed. The effects of the tip speed and superficial gas velocity on the particle flow have been analysed and quantified in terms of the flow energy, strain rate and stresses. The main results from the present study are summarised as follows:

- (1) In the packed bed state, the gas pressure drop in the downward test has the same value as the permeability test without impeller motion. The effect of gas flow on the flow energy of particles can be accounted for by a multiplying factor reducing the incremental flow energy in vacuum when an upward fluid drag prevails.
- (2) The strain rate in front of blade is not uniform along the blade length, with the largest value found in the tip region

- and the lowest value in the shaft region. Its value is mainly determined by the tip speed, and is not sensitive to the particle size and gas flow considered in this work.
- (3) Both the flow energy and stresses are functions of the strain rate and permeating air. They increase with the strain rate and decrease significantly with the gas flow. The flow energy correlates well with the shear stress in front of the blade for all conditions including permeating air, and the latter is a linear function of strain rate, this representing a constitutive law for powder flow in the intermediate flow regime.

## Acknowledgments

The authors are grateful to Science Fund for Creative Research Groups of the National Natural Science Foundation of China (Grant No. 51121092) and the scholarship from China Scholarship Council (CSC) (Grant No. 201506280088) for the first author. We are thankful to DEM Solutions, Edinburgh, UK, for providing a special license for the EDEM software for use in this work, and also to Drs Colin Hare and Mehrdad Pasha for their generous help in setting up the computational facility. We also thank Freeman Technology for making available an FT4 instrument for the experiment, as well as technical support from Dr Doug Millington-Smith.

## References

- Bharadwaj, R., Ketterhagen, W.R., Hancock, B.C., 2010. Discrete element simulation study of a Freeman powder rheometer. *Chem. Eng. Sci.* 65, 5747–5756.
- Bruni, G., Barletta, D., Poletto, M., Lettieri, P., 2007. A rheological model for the flowability of aerated fine powders. *Chem. Eng. Sci.* 62, 397–407.
- Campbell, C.S., 2004. Granular flows and gas fluidization. *Int. J. Chem. Reactor Eng.* 2.
- Campbell, C.S., 2006. Granular material flows – an overview. *Powder Technol.* 162, 208–229.
- Carson, J.W., 2015. Limits of silo design codes. *Practi. Period. Struct. Des. Constr.* 20, 04014030.
- Chialvo, S., Sun, J., Sundaresan, S., 2012. Bridging the rheology of granular flows in three regimes. *Phys. Rev. E: Stat., Nonlin., Soft Matter Phys.* 85, 021305.
- Cundall, P.A., Strack, O.D.L., 1979. A discrete numerical model for granular assemblies. *Géotechnique* 29, 47–65.
- da Cruz, F., Emam, S., Prochnow, M., Roux, J.N., Chevoir, F., 2005. Rheophysics of dense granular materials: discrete simulation of plane shear flows. *Phys. Rev. E: Stat., Nonlin., Soft Matter Phys.* 72, 021309.
- DallaValle, J.M., 1948. Micromeritics: The Technology of Fine Particles. Pitman, New York.
- Delannay, R., Louge, M., Richard, P., Taberlet, N., Valance, A., 2007. Towards a theoretical picture of dense granular flows down inclines. *Nat. Mater.* 6, 99–108.
- Di Felice, R., 1994. The voidage function for fluid-particle interaction systems. *Int. J. Multiph. Flow* 20, 153–159.
- Enstad, G., 1975. On the theory of arching in mass flow hoppers. *Chem. Eng. Sci.* 30, 1273–1283.
- Freeman, R., 2007. Measuring the flow properties of consolidated, conditioned and aerated powders – a comparative study using a powder rheometer and a rotational shear cell. *Powder Technol.* 174, 25–33.
- Gutam, K.J., Mehandia, V., Nott, P.R., 2013. Rheometry of granular materials in cylindrical Couette cells: Anomalous stress caused by gravity and shear. *Phys. Fluids* 25, 070602.
- Han, X., Ghorai, C., To, D., Chen, Y., Dave, R., 2011. Simultaneous micronization and surface modification for improvement of flow and dissolution of drug particles. *Int. J. Pharm.* 415, 185–195.
- Hare, C., Ghadiri, M., Dennehy, R., 2011. Prediction of attrition in agitated particle beds. *Chem. Eng. Sci.* 66, 4757–4770.
- Hare, C., Zafar, U., Ghadiri, M., Freeman, T., Clayton, J., Murtagh, M.J., 2015. Analysis of the dynamics of the FT4 powder rheometer. *Powder Technol.* 285, 123–127.
- Hare, C.L., Ghadiri, M., 2013. Influence of measurement cell size on predicted attrition by the Distinct Element Method. *Powder Technol.* 236, 100–106.
- Hua, X., Curtis, J., Guo, Y., Hancock, B., Ketterhagen, W., Wassgren, C., 2015. The internal loads, moments, and stresses in rod-like particles in a low-speed, vertical axis mixer. *Chem. Eng. Sci.* 134, 581–598.
- Hua, X., Curtis, J., Hancock, B., Ketterhagen, W., Wassgren, C., 2013. The kinematics of non-cohesive, spherocylindrical particles in a low-speed, vertical axis mixer. *Chem. Eng. Sci.* 101, 144–164.
- Jenike, A.W., 1961. Gravity Flow of Bulk Solids. Bulletin No. 108. Utah State University.
- Jenkins, J.T., 2006. Dense shearing flows of inelastic disks. *Phys. Fluids* 18, 103307.
- Jop, P., Forterre, Y., Pouliquen, O., 2006. A constitutive law for dense granular flows. *Nature* 441, 727–730.
- Khaliltehrani, M., Abrahamsson, P.J., Rasmuson, A., 2013. The rheology of dense granular flows in a disc impeller high shear granulator. *Powder Technol.* 249, 309–315.
- Khaliltehrani, M., Gomez-Fino, E.M., Abrahamsson, P.J., Rasmuson, A., 2015. Continuum modeling of multi-regime particle flows in high-shear mixing. *Powder Technol.* 280, 67–71.
- Kinnunen, H., Hebbink, G., Peters, H., Shur, J., Price, R., 2014. An investigation into the effect of fine lactose particles on the fluidization behaviour and aerosolization performance of carrier-based dry powder inhaler formulations. *AAPS PharmSciTech* 15, 898–909.
- Klein, J., Hohne, D., Husemann, K., 2003. The influence of air permeation on the flow properties of bulk solids. *Chem. Eng. Technol.* 26, 139–146.
- Koval, G., Roux, J.N., Corfdir, A., Chevoir, F., 2009. Annular shear of cohesionless granular materials: from the inertial to quasistatic regime. *Phys. Rev. E: Stat., Nonlin., Soft Matter Phys.* 79, 021306.
- Kumar, V.S., Murthy, T., Nott, P.R., 2013. Rheometry of dense granular materials: the crucial effects of gravity and confining walls. *Powders Grains* 2013 (1542), 49–51.
- Langroudi, M.K., Turek, S., Ouazzi, A., Tardos, G.I., 2010. An investigation of frictional and collisional powder flows using a unified constitutive equation. *Powder Technol.* 197, 91–101.
- Leturia, M., Benali, M., Lagarde, S., Ronga, I., Saleh, K., 2014. Characterization of flow properties of cohesive powders: a comparative study of traditional and new testing methods. *Powder Technol.* 253, 406–423.
- Luding, S., 2008. Constitutive relations for the shear band evolution in granular matter under large strain. *Particuology* 6, 501–505.
- MiDi, G.D.R., 2004. On dense granular flows. *Eur Phys J E Soft Matter* 14, 341–365.
- Mort, P., Michaels, J.N., Behringer, R.P., Campbell, C.S., Kondic, L., Langroudi, M.K., Shattuck, M., Tang, J., Tardos, G.I., Wassgren, C., 2015. Dense granular flow – a collaborative study. *Powder Technol.* 284, 571–584.
- Nan, W., Wang, Y., Wang, J., 2016. Numerical analysis on the fluidization dynamics of rodlike particles. *Adv. Powder Technol.* 27, 2265–2276.
- Nan, W.G., Wang, Y.S., Ge, Y., Wang, J.Z., 2014. Effect of shape parameters of fiber on the packing structure. *Powder Technol.* 261, 210–218.
- Nan, W.G., Wang, Y.S., Liu, Y.W., Tang, H.P., 2015. DEM simulation of the packing of rodlike particles. *Adv. Powder Technol.* 26, 527–536.
- Osorio, J.G., Muzzio, F.J., 2013. Effects of powder flow properties on capsule filling weight uniformity. *Drug Dev. Ind. Pharm.* 39, 1464–1475.
- Pasha, M., Hare, C., Hassanpour, A., Ghadiri, M., 2013. Analysis of ball indentation on cohesive powder beds using distinct element modelling. *Powder Technol.* 233, 80–90.
- Pouliquen, O., Cassar, C., Jop, P., Forterre, Y., Nicolas, M., 2006. Flow of dense granular material: towards simple constitutive laws. *J. Stat. Mech. Theory Exp.* 2006, P07020.
- Remy, B., Khinast, J.G., Glasser, B.J., 2009. Discrete element simulation of free flowing grains in a four-bladed mixer. *AIChE J.* 55, 2035–2048.
- Remy, B., Khinast, J.G., Glasser, B.J., 2011. Polydisperse granular flows in a bladed mixer: experiments and simulations of cohesionless spheres. *Chem. Eng. Sci.* 66, 1811–1824.
- Rong, L.W., Dong, K.J., Yu, A.B., 2013. Lattice-Boltzmann simulation of fluid flow through packed beds of uniform spheres: effect of porosity. *Chem. Eng. Sci.* 99, 44–58.
- Savage, S.B., 1998. Analyses of slow high-concentration flows of granular materials. *J. Fluid Mech.* 377, 1–26.
- Schwendes, J., 2003. Review on testers for measuring flow properties of bulk solids (based on an IFPRI-Report 1999). *Granular Matter* 5, 1–43.
- Shur, J., Harris, H., Jones, M.D., Kaerger, J.S., Price, R., 2008. The role of fines in the modification of the fluidization and dispersion mechanism within dry powder inhaler formulations. *Pharm. Res.* 25, 1631–1640.
- Tang, J., Behringer, R.P., 2011. How granular materials jam in a hopper. *Chaos* 21, 041107.
- Tardos, G.I., 1997. A fluid mechanistic approach to slow, frictional flow of powders. *Powder Technol.* 92, 61–74.
- Tardos, G.I., McNamara, S., Talu, I., 2003. Slow and intermediate flow of a frictional bulk powder in the Couette geometry. *Powder Technol.* 131, 23–39.
- Tomasetta, I., Barletta, D., Lettieri, P., Poletto, M., 2012. The measurement of powder flow properties with a mechanically stirred aerated bed. *Chem. Eng. Sci.* 69, 373–381.
- Vasilenko, A., Glasser, B.J., Muzzio, F.J., 2011. Shear and flow behavior of pharmaceutical blends – method comparison study. *Powder Technol.* 208, 628–636.
- Wang, C., Hassanpour, A., Ghadiri, M., 2008. Characterisation of flowability of cohesive powders by testing small quantities of weak compacts. *Particuology* 6, 282–285.
- Wu, C.Y., Guo, Y., 2012. Numerical modelling of suction filling using DEM/CFD. *Chem. Eng. Sci.* 73, 231–238.
- Xiong, Q., Aramideh, S., Passalacqua, A., Kong, S.-C., 2015. Characterizing effects of the shape of screw conveyors in gas-solid fluidized beds using advanced numerical models. *J. Heat Transfer* 137, 061008.
- Xiong, Q., Madadi-Kandjani, E., Lorenzini, G., 2014. A LBM-DEM solver for fast discrete particle simulation of particle-fluid flows. *Continuum Mech. Thermodyn.* 26, 907–917.
- Zhou, Q., Armstrong, B., Larson, I., Stewart, P.J., Morton, D.A., 2010a. Improving powder flow properties of a cohesive lactose monohydrate powder by intensive mechanical dry coating. *J. Pharm. Sci.* 99, 969–981.
- Zhou, Q.T., Armstrong, B., Larson, I., Stewart, P.J., Morton, D.A., 2010b. Understanding the influence of powder flowability, fluidization and agglomeration characteristics on the aerosolization of pharmaceutical model powders. *Eur. J. Pharm. Sci.* 40, 412–421.
- Zhou, Z.Y., Kuang, S.B., Chu, K.W., Yu, A.B., 2010c. Discrete particle simulation of particle-fluid flow: model formulations and their applicability. *J. Fluid Mech.* 661, 482–510.